Received 24 November 2021; revised 21 December 2021; accepted 14 January 2022. Date of publication 18 January 2022; date of current version 22 February 2022. The review of this article was arranged by Editor C. Surya.

Digital Object Identifier 10.1109/JEDS.2022.3143999

Compact Millimeter-Wave On-Chip Dual-Band Bandpass Filter in 0.15-μm GaAs Technology

KAI-DA XU[1] (Senior Member, IEEE), SHENGPEI XIA[1], YANNAN JIANG[2] (Member, IEEE), YING-JIANG GUO[3] (Member, IEEE), YIQUN LIU[1] (Student Member, IEEE), RUI WU[4], JIANLEI CUI[5], AND QIANG CHEN[6] (Senior Member, IEEE)

1 School of Information and Communications Engineering, Xi'an Jiaotong University, Xi'an 710049, China
2 Guangxi Key Laboratory of Wireless Wideband Communication and Signal Processing, Guilin University of Electronic Technology, Guilin 541004, China
3 Microsystem and Terahertz Research Center, China Academy of Engineering Physics, Chengdu 610200, China
4 National Key Laboratory of Microwave Imaging Technology, Aerospace Information Research Institute, Chinese Academy of Science, Beijing 100094, China
5 State Key Laboratory for Manufacturing Systems Engineering, Xi'an Jiaotong University, Xi'an 710049, China
6 Department of Communications Engineering, Tohoku University, Sendai 980-8579, Japan

CORRESPONDING AUTHORS: Y. JIANG AND Y.-J. GUO (e-mail: ynjiang@guet.edu.cn; guoyingjiang1@gmail.com)

This work was supported in part by the Natural Science Foundation of Guangxi under Grant 2019GXNSFFA245002; in part by the NSAF Joint Fund under Grant U2130102; in part by the State Key Laboratory of Advanced Optical Communication Systems Networks under Grant 2022GZKF020; and in part by the "Siyuan Scholar" Fellowship of XJTU.

ABSTRACT A compact on-chip dual-band bandpass filter (BPF) at millimeter-wave frequencies is proposed in 0.15-μm GaAs technology. To understand the working mechanism of the BPF, an LC equivalent circuit model is presented and analyzed for position estimation of the transmission zeros and poles. For demonstration, an on-chip BPF example is fabricated and tested, whose simulation and measurement are in good agreement. There are two frequency bands at 60.2 and 79.7 GHz with bandwidths of 9% and 6.8%, respectively. The chip, excluding the feedings, is only 0.304 mm $\times$ 0.464 mm.

INDEX TERMS Bandpass filters, dual-band, GaAs-based circuits, millimeter wave circuits, on-chip devices.

I. INTRODUCTION

With the development of new generation multi-service wireless communication systems, millimeter-wave multi-band bandpass filters (BPFs) have attracted increasing attention recently. Although various design methods for millimeter-wave BPFs have been presented including on-chip planar structures [1]–[11] and waveguide configurations [12]–[14], most of them are with only single band. So far, there has been little research on dual-band or even multi-band BPFs using semiconductor technology at millimeter-wave frequencies.

In [15] and [16], substrate integrated waveguides were employed to construct resonant cavities for the design of dual-band BPFs, whose approach was similar to designing waveguide filters in [13], [14]. However, the sizes of these waveguide devices are inherently bulky, and they are difficult to integrate with some other front-end modules for the final system-in-package (SiP) or system on a chip (SoC). In contrast, the on-chip BPFs using SiGe, GaAs and CMOS with single frequency band [1]–[8] and dual-band [9]–[11] are readily useful due to the advantages of small sizes and ease of integration. In [9], a dual-band on-chip BPF at 24 and 60 GHz using a 0.18-μm standard CMOS process was designed through loading several quarter-wavelength stepped-impedance resonators. Thus, the die area of the BPF would result in a relatively large size. Similarly, the works in [10] and [11] suffered from the same issue, where both of the coupled lines and stubs were of quarter wavelength and especially the coupled-line unit could not be meandered for the implementation. Moreover, the transmission zeros (TZs) and transmission poles (TPs) could not be controlled independently. Therefore, the multi-band on-chip BPFs with small sizes and ease of design are urgently needed to save the cost of the radio-frequency integrated circuits (RFICs).

In [2], we previously presented a single-band BPF using 0.15-μm GaAs technology. In order to extend to the dual-band application using the same semiconductor manufacturing process, a millimeter-wave on-chip dual-band BPF

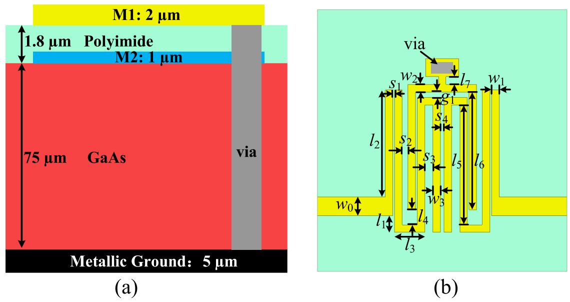

FIGURE 1. **(a) Stack-up of the employed 0.15-μm GaAs pHEMT technology, where the relative dielectric constants of the GaAs and polyimide films are 12.9 and 2.9, respectively. (b) Proposed compact dual-band BPF, where $l_1 = 45$ μm, $l_2 = 285$ μm, $l_3 = 80$ μm, $l_4 = 40$ μm, $l_5 = 320$ μm, $l_6 = 315$ μm, $l_7 = 21$ μm, $w_0 = 50$ μm, $w_1 = w_2 = w_3 = 20$ μm, $s_1 = 5$ μm, $s_2 = 15$ μm, $s_3 = 22$ μm, $s_4 = 10$ μm, and $g_1 = 15$ μm.**

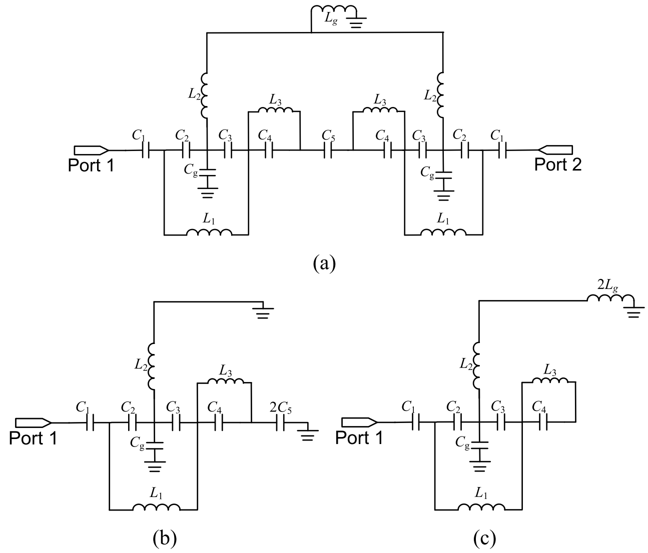

FIGURE 2. **(a) LC equivalent circuit model of the designed BPF, and its (b) odd mode and (c) even mode equivalent circuits.**

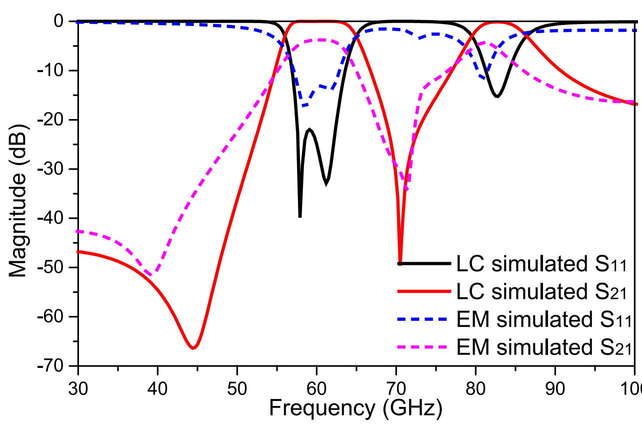

FIGURE 3. **EM and LC equivalent circuit simulations, where the parameters in Fig. 2 are as follows: $L_1 = 170$ pH, $L_2 = 65.4$ pH, $L_3 = 32$ pH, $L_g = 9.2$ pH, $C_1 = 26.7$ fF, $C_2 = 51$ fF, $C_3 = 76.8$ fF, $C_4 = 159$ fF, $C_5 = 16.8$ fF, and $C_g = 30$ Ff.**

is designed in this paper with two TZs and three TPs. The positions of TZs and TPs can be easily tuned, thereby controlling the center frequencies and bandwidths of the passbands. The fabricated filter possesses low insertion loss and compact size with dual-band frequency response.

II. DESIGN OF ON-CHIP DUAL-BAND BPF

Fig. 1(a) shows the stack-up of the standard 0.15-μm GaAs pHEMT technology, where two metal layers M1 and M2 with the thicknesses of 2 μm and 1 μm, respectively, are available for circuit design, and their conductivities are both 4×10^7 S/m. A compact dual-band BPF is designed on M1 layer using this GaAs technology, as illustrated in Fig. 1(b).

The working mechanism of the designed BPF filter can be analyzed by an *LC* equivalent circuit model in Fig. 2(a). The metal strips with lengths of $(l_3 + l_5 + 2w_3)$ and $(s_3 + l_5 + 2w_3)$ are assumed as an inductor L_1 and an inductor L_3, respectively. The inverted L-shaped metal strip connected with the via hole is represented by an inductors L_2. The gap couplings between the closely spaced metal strips are equivalently demonstrated by nine capacitors (i.e., two C_1, two C_2, two C_3, two C_4 and a C_5). The capacitor C_g accounts for the electrical coupling between the metal strip and the ground. The short metal strip connected to the square via together with the via itself can be regarded as an inductor L_g, which is short-circuited to the ground.

The comparisons between the simulation results of EM model (i.e., Fig. 1(b)) and *LC* circuit model are shown in Fig. 3, where reasonable agreement is obtained. Both of them have two TZs and three TPs, two of which at the first frequency band and the third one at the second frequency band. The circuit in Fig. 2(a) can be bisected into two halves along the central plane due to the symmetry and then the odd- and even-mode analysis method can be adopted, as shown in Fig. 2(b) and 2(c). The reflection coefficient S_{11} and transmission coefficient S_{21} of the proposed BPF are dependent on the input impedances of odd-mode and even-mode equivalent circuits Z_{odd} and Z_{even}, by calculating the following equations.

$$S_{11} = \frac{\Gamma_e + \Gamma_o}{2} = \frac{Z_{even}Z_{odd} - Z_0^2}{(Z_{even} + Z_0)(Z_{odd} + Z_0)} \quad (1)$$

$$S_{21} = \frac{\Gamma_e - \Gamma_o}{2} = \frac{Z_0(Z_{even} - Z_{odd})}{(Z_{even} + Z_0)(Z_{odd} + Z_0)} \quad (2)$$

Then, the TPs and TZs can be determined by setting $S_{11} = 0$ and $S_{21} = 0$ through (1) and (2), respectively.

Table 1 tabulates the variations of TPs and TZs against different values of the inductors and capacitors in Fig. 2 for better understanding the tunable abilities of the TZs and TPs. The brown blocks represent that TP or TZ almost remains unchanged as the *LC* parameter is varied. The purple blocks represent that the positions of TP or TZ slightly change when the *LC* parameter is tuned. Moreover, the orange block

TABLE 1. Relationships between parameters and TZs or TPs.

	L_1	L_2	L_3	L_g	C_1	C_2	C_3	C_4	C_5	C_g
f_{z1}	↘	—	—	—	—	↘	—	—	↘	—
f_{p1}	—	—	↘	—	—	↘	—	↘	↘	—
f_{p2}	↗	—	↘	—	—	—	—	↘	—	—
f_{z2}	—	—	↘	—	—	—	—	↘	—	—
f_{p3}	—	↘	—	—	—	—	—	—	—	↘

—: not much impact; ↗: positive correlation; ↘: negative correlation.

and blue blocks denote the positive and negative correlations, respectively, for the relations between the *LC* and TP/TZ. With this table, it gives an overall guidance for tuning the design specifications of the center frequency, fractional bandwidth and out-of-band rejection.

More specifically, when the value of L_1 increases from 164 pH to 176 pH, the first TZ f_{z1} will be adjusted from 49 GHz to 43 GHz while the other TZ and TPs keep fixed, as illustrated in Fig. 4(a), thus the bandwidth of the first frequency band will be increased accordingly. Similarly, the inductor L_3 can control the position of the second TZ f_{z2}, thereby changing the bandwidth as shown in Fig. 4(b). Therefore, the bandwidth of the first passband can be tuned by adjusting the inductor L_1 or L_3. Furthermore, when the values of L_1 and L_3 are adjusted simultaneously, the two TZs will both be moved, resulting in the adjustment of the center frequency of the first passband, as shown in Fig. 4(c). Interestingly, the center frequency of the second passband almost remains unchanged, which means that the first passband can be adjusted independently. On the other hand, the third TP f_{p3} can be manipulated by tuning the value of L_2, thus the center frequency of the second passband will be controlled accordingly without affecting the first passband, as demonstrated in Fig. 4(d).

The classical resonator filter theory can be applied to explain the generation mechanism of TPs and TZs. Fig. 5 illustrates the frequency responses of $|S_{11}|$ results for the three circuit structures in the inset. As can be seen, the pair of meander line structure in the left inset consists of two identical microstrip resonators, thus it can generate two TPs within the first passband through input/output port feeding. For the grounded U-shaped structure in the right inset of Fig. 5, it can be seen as the short stub-loaded resonator [17] with input/output port feeding, which has two transmission poles, each one at the first and second passbands. When these two structures are combined together to construct the proposed dual-band BPF, there should be three TPs at the first passband and one TP at the second passband theoretically. But due to the coupling between the pair of meander line structure and the grounded U-shaped structure, one of three TPs is moved to around 72 GHz instead of locating at the first passband. This phenomenon may be caused by interaction between closely spaced resonant structures, resulting in the change of effective electrical length of the

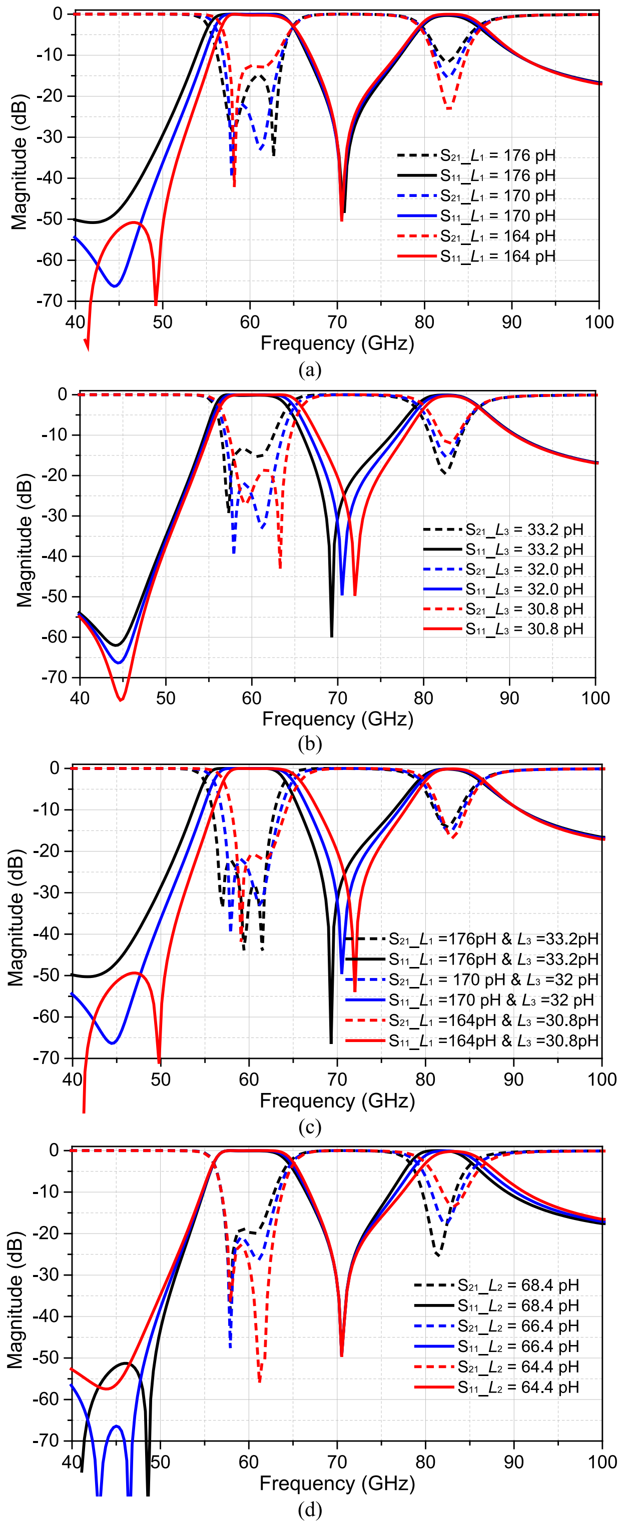

FIGURE 4. Simulated S-parameters with different values of (a) L_1, (b) L_3, (c) L_1 & L_3, and (d) L_2.

resonance for one of three TPs. Fortunately, the performance of the filter is not deteriorated significantly.

For the physical dimensions in Fig. 1(b), the parameters l_5 and g_1 can be independently tuned to control the center

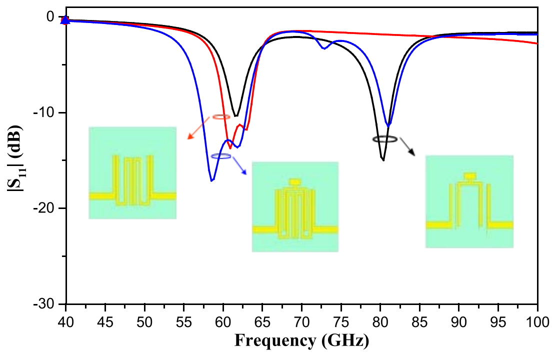

FIGURE 5. Simulated $|S_{11}|$ of the filter without grounded U-shaped structure (left inset figure), the proposed dual-band BPF (middle inset figure), and the filter without a pair of meander line structure (right inset figure).

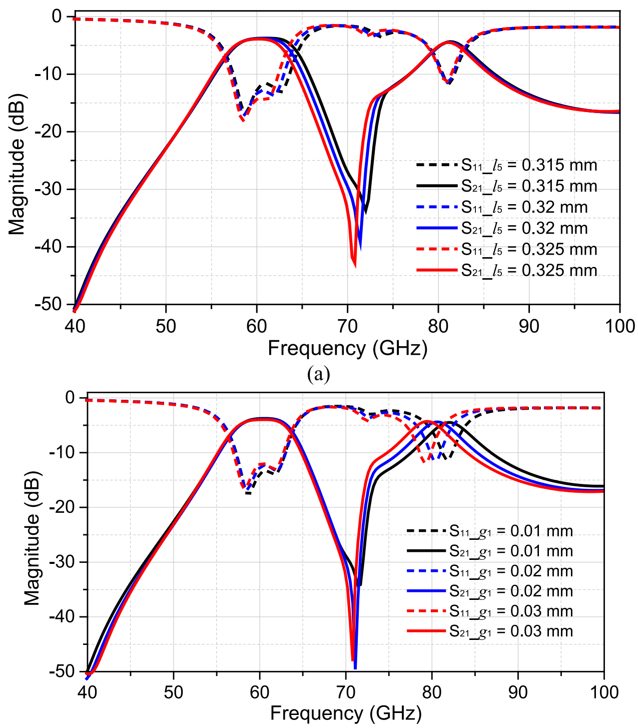

(a)

(b)

FIGURE 6. Simulated S-parameters with different values of (a) l_5 and (b) g_1. The other default physical dimensions of the proposed BPF are the same as the ones in the caption of Fig. 1.

frequency and bandwidth of the first passband and second passband, respectively. As shown in Fig. 6(a), when the value of the length l_5 increases from 0.315 mm to 0.325 mm, the TZ between two passbands will be adjusted from 70.2 GHz to 72.3 GHz while the other one TZ remains fixed. Thus, the center frequency and bandwidth of the first passband of the BPF can be easily manipulated accordingly by tuning the value of l_5. For the second passband, as illustrated in Fig. 6(b), the center frequency can be also independently tuned with the change of the value g_1.

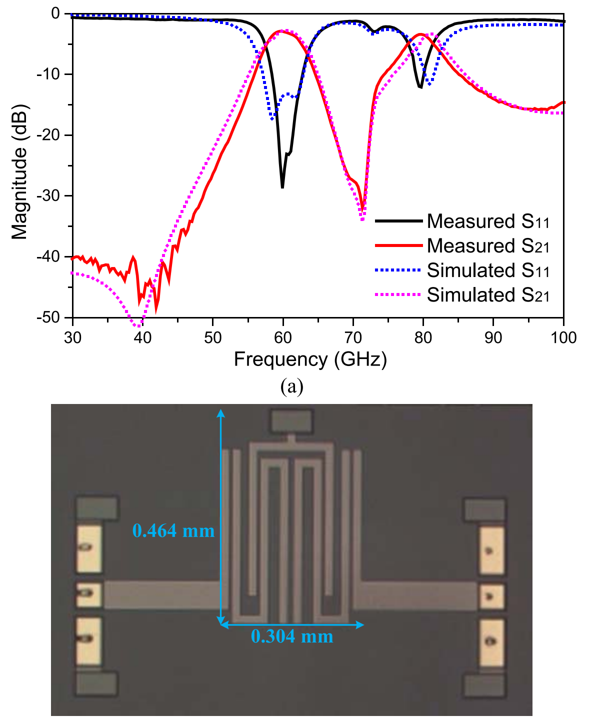

(a)

(b)

FIGURE 7. (a) Simulated and measured results, and (b) die photo of the proposed dual-band BPF.

III. ON-WAFER MEASUREMENTS

For further demonstration of the proposed dual-band BPF, an example is fabricated and then measured via an on-wafer ground-signal-ground probing using a vector network analyzer. As seen in Fig. 7(a), the measured results of *S*-parameters of the dual-band BPF agree reasonably well with the simulations of EM model. The measurements show that it has two passbands, one center frequency of which is at 60.2 GHz with a 3-dB bandwidth from 57.5 to 62.9 GHz (9%) and the other one is at 79.7 GHz with a 3-dB bandwidth from 77 to 82.4 GHz (6.8%). The minimum insertion losses (ILs) within the two passbands are 2.8 dB and 3.0 dB, respectively. The return losses within the two passbands are better than 13 dB and 10 dB, respectively.

The die photograph of the designed dual-band BPF is shown in Fig. 7(b). The chip size, excluding the feedings, is only 0.304 mm × 0.464 mm. The performance comparisons with some recently reported dual-band BPFs have been tabulated in Table 2. As can be seen, the proposed dual-band BPF has the advantages of low ILs and small chip size.

IV. CONCLUSION

A compact on-chip dual-band BPF at 60 and 80 GHz using GaAs pHEMT technology has been presented with a simple design topology. The LC equivalent circuit model is used to understand the working mechanism of the BPF and analyze positions of the TZs and TPs. Due to its very compact size, low in-band ILs and moderate bandwidth,

TABLE 2. Performance comparisons with some previous dual-band BPFs.

	f_1/f_2 (GHz)	TZs	Δf (%)	IL (dB)	Size (mm^2)	Tech.
[9]	24/60	2	NM*	3.6/2.8	1.03 × 0.59	0.18 µm CMOS
[10]	35/70	3	32.9/ 22.4	3.0/3.3	1.489 × 0.650	0.35 µm BiCMOS
[11]	28/50	4	39.3/ 5	0.58/3. 29	0.535 × 0.686	GaAs IPD
[15]	20/21.5	4	2.4/2 .5	2.84/2. 03	24.26 × 23.84	SIW on the PCB
This work	**60.2/79.7**	**2**	**9/6.8**	**2.8/3.0**	**0.304 × 0.464**	**0.15 µm GaAs**

*NM: Not Mentioned.

the proposed BPF is readily applied for 5G multi-service wireless communication systems.

REFERENCES

[1] Y. Yang, H. Liu, Z. J. Hou, X. Zhu, E. Dutkiewicz, and Q. Xue, "Compact on-chip bandpass filter with improved in-band flatness and stopband attenuation in 0.13-µm (Bi)-CMOS technology," *IEEE Electron Device Lett.*, vol. 38, no. 10, pp. 1359–1362, Oct. 2017.

[2] K.-D. Xu, Y.-J. Guo, Y. Liu, X. Deng, Q. Chen, and Z. Ma, "60-GHz compact dual-mode on-chip bandpass filter using GaAs technology," *IEEE Electron Device Lett.*, vol. 42, no. 8, pp. 1120–1123, Aug. 2021.

[3] J. Liang, H. Zhang, D. Zhang, H. Zhang, and W. Pang, "Lamb wave AlN micromechanical filters integrated with on-chip capacitors for RF front-end architectures," *IEEE J. Electron Devices Soc.*, vol. 3, no. 4, pp. 361–364, Jul. 2015.

[4] M. Li, Y. Yang, K. D. Xu, X. Zhu, and S. W. Wong, "Microwave on-chip bandpass filter based on hybrid coupling technique," *IEEE Trans. Electron Devices*, vol. 65, no. 12, pp. 5453–5459, Dec. 2018.

[5] Y.-J. Guo, K.-D. Xu, X. Deng, X. Cheng, and Q. Chen, "Millimeter-wave on-chip bandpass filter based on spoof surface plasmon polaritons," *IEEE Electron Device Lett.*, vol. 41, no. 8, pp. 1165–1168, Aug. 2020.

[6] K.-D. Xu, X. Zhu, Y. Yang, and Q. Chen, "A broadband on-chip bandpass filter using shunt dual-layer meander-line resonators," *IEEE Electron Device Lett.*, vol. 41, no. 11, pp. 1617–1620, Nov. 2020.

[7] H. R. Zhu, X. Y. Ning, Z. X. Huang, and X. L. Wu, "An ultra-compact on-chip reconfigurable bandpass filter with semi-lumped topology by using GaAs pHEMT technology," *IEEE Access*, vol. 8, pp. 31606–31613, 2020.

[8] X.-J. Liu, W. Wu, K.-D. Xu, Y.-J. Guo, and Q. Chen, "60-GHz half-mode substrate integrated waveguide bandpass filter in 0.15-µm GaAs technology," *Front. Phys.*, vol. 9, Nov. 2021, Art. no. 774338.

[9] L.-K. Yeh, C.-Y. Hsu, C.-Y. Chen, and H.-R. Chuang, "A 24-/60-GHz CMOS on-chip dual-band bandpass filter using trisection dual-behavior resonators," *IEEE Electron Device Lett.*, vol. 29, no. 12, pp. 1373–1375, Dec. 2008.

[10] V. N. R. Vanukuru and V. K. Velidi, "CMOS 35/70 GHz dual-band bandpass filter with five transmission zeros using compact stub-loaded coupled-line unit," in *Proc. IEEE MTT-S Int. Microw. RF Conf. (IMARC)*, 2019, pp. 1–3.

[11] G. Shen, W. Feng, W. Che, Y. Shi, and Y. Shen, "Millimeter-wave dual-band bandpass filter with large bandwidth ratio using GaAs-based integrated passive device technology," *IEEE Electron Device Lett.*, vol. 42, no. 4, pp. 493–496, Apr. 2021.

[12] K.-D. Xu, S. Xia, Y. Guo, J. Cui, A. Zhang, and Q. Chen, "W-band E-plane waveguide bandpass filter based on meander ring resonator," *IEEE Microw. Wireless Compon. Lett.*, vol. 31, no. 12, pp. 1267–1270, Dec. 2021.

[13] J. Y. Jin, X. Q. Lin, and Q. Xue, "A novel dual-band bandpass E-plane filter using compact resonators," *IEEE Microw. Wireless Compon. Lett.*, vol. 26, no. 7, pp. 484–486, Jul. 2016.

[14] K. Zhou, J.-Q. Ding, C.-X. Zhou, and W. Wu, "W-band dual-band quasi-elliptical waveguide filter with flexibly allocated frequency and bandwidth ratios," *IEEE Microw. Wireless Compon. Lett.*, vol. 28, no. 3, pp. 206–208, Mar. 2018.

[15] K. Zhou, C.-X. Zhou, and W. Wu, "Substrate-integrated waveguide dual-band filters with closely spaced passbands and flexibly allocated bandwidths," *IEEE Trans. Compon. Packag. Manuf. Technol.*, vol. 8, no. 3, pp. 465–472, Mar. 2018.

[16] K. Dong, J. Mo, Y. He, Z. Ma, and X. Yang, "Design of a millimeter-wave dual-band bandpass filter using SIW dual-mode cavities," in *Proc. IEEE MTT-S Int. Wireless Symp. (IWS)*, 2016, pp. 1–3.

[17] F.-C. Chen, Q.-X. Chu, and Z.-H. Tu, "Design of compact dual-band bandpass filter using short stub loaded resonator," *Microw. Opt. Technol. Lett.*, vol. 51, no. 4, pp. 959–963, 2009.